

Intensity Fluctuation Spectra as a Design Guide for Nonlinear-Tolerant Constellation Shaping

Ravneel Prasad, *Student Member, IEEE*, Emanuele Viterbo, *Fellow, IEEE*

Abstract—Nonlinearity in coherent fiber links is fundamentally driven by the temporal statistics and spectral structure of signal intensity. This paper develops a unified framework that links block-level energy statistics of shaped constellations to the low-frequency features of the intensity-fluctuation power spectral density (PSD), thereby enabling spectral–temporal co-design for nonlinear mitigation. A semi-analytical PSD model is derived for finitely block-shaped symbols (including Constant Composition Distribution Matching (CCDM) and Enumerative Sphere Shaping (ESS)), explicitly exposing contributions from self-beating dependent on symbol energy variance, inter-symbol beating dependent on mean symbol energy, and block-induced energy variance terms. A compact expression for the spectral-dip width is obtained that captures the block length, symbol rate, pulse roll-off, and chromatic dispersion. This yields design rules for lowering the low-frequency content. The low-frequency content most strongly drives the induced XPM. Resulting optimal symbol-rate laws are provided for shaped and unshaped systems, and are validated by Monte-Carlo simulations, which also confirm the distinct low-frequency behaviour of CCDM (suppressed DC) versus ESS (finite DC pedestal at moderate block lengths). The framework consolidates prior time- and frequency-domain views and supplies actionable guidance for choosing block length, symbol rate, and shaping method to reduce nonlinear interference in high-capacity WDM systems.

Index Terms—Cross-Phase Modulation, Fiber Nonlinearity, Intensity Fluctuations, Kerr Effect, Nonlinear Interference, Nonlinear Tolerance, Optical Communications, Probabilistic Amplitude Shaping, Sphere Shaping

I. INTRODUCTION

Constellation shaping is a crucial technique for enhancing optical communication systems [1]–[4]. By optimizing the probability or position of transmitted symbols, it uses signal space more efficiently, which improves energy efficiency and reduces nonlinear impairments. In standard AWGN channels, shaping provides up to 1.53 dB of SNR gain [3]–[6]. However, fiber-optic channels can exceed this limit with appropriate shaping [2], [5]. This is achieved by lowering the energy variance of the signal to reduce nonlinear phase noise, while simultaneously lowering the average energy to increase the linear gain [4], [5]. This variance reduction significantly impacts the low-frequency components of the intensity fluctuation spectra [7].

Probabilistic shaping has attracted significant interest due to its compatibility with existing QAM architectures, as it does not require modification to the constellation geometry [8]. Crucially, it enables rate adaptivity, allowing systems with

fixed Forward Error Correction (FEC) to meet performance targets under varying channel conditions [8], [9]. The shaping process relies on a *distribution matcher* to map information bits onto symbol sequences following a target distribution. To limit computational complexity, these matchers are typically implemented using fixed block lengths [3], [10]. Consequently, the impact of block length on fiber nonlinearity has been the subject of extensive study [1], [3], [4], [11]–[13].

Cross-Phase Modulation (XPM) is fundamentally driven by intensity fluctuations (IFs) evolving along dispersive fibers [14], [15]. Since XPM efficiency exhibits a low-pass characteristic determined by fiber parameters and channel separation, low-frequency IF components act as the dominant source of nonlinear interference [15]. Recent spectral modeling [7] suggests that these spectra can be engineered by suppressing specific symbol beat components. This concept was practically demonstrated in [16], [17], where Manchester Coding and direct-sequence spread spectrum techniques were employed to attenuate low-frequency IFs. The resulting reduction in XPM penalties corroborates the critical impact of low-frequency intensity dynamics on system performance [15].

Complementary research has addressed intensity fluctuations through the lens of super-symbol transmission schemes [10], [18]. By grouping components into four-dimensional dual-polarization super-symbols, these methods constrain joint energy and minimize instantaneous power variations across polarizations. This multidimensional shaping improves nonlinear tolerance compared to standard one- or two-dimensional approaches by increasing the degrees of freedom available to control energy statistics. Furthermore, the interplay between block length and symbol rate has been shown to induce a spectral dip in the intensity fluctuation spectrum near DC, where a wider dip serves as a predictor for improved nonlinear performance [10].

The Energy Dispersion Index (EDI) was proposed to quantify temporal energy unevenness by calculating the normalized variance of energy within fixed-duration windows [19]. Acting as a metric for signal “burstiness”, lower EDI values correlate with improved nonlinear tolerance, supporting the intuition that suppressing low-frequency power fluctuations mitigates impairments. However, while EDI effectively highlights the role of energy statistics—consistent with the analysis of fourth-order moments in [20]—it remains a heuristic measure lacking explicit spectral insight. Bridging this gap, recent work has demonstrated that the Power Spectral Density (PSD) of the energy signal is intrinsically governed by these temporal statistics and can be analytically linked to phase noise via a perturbation-based linear filter model [2]. These findings align with observations in [10], [18], confirming that low-

This work was supported by The Faculty of Engineering Postgraduate Publication Award, Monash University.

The authors are with the Department of Electrical and Computer Systems Engineering, Monash University, Clayton, VIC 3800, Australia (e-mail: ravneel.prasad@monash.edu; emanuele.viterbo@monash.edu).

frequency intensity components are the dominant contributors to nonlinear phase noise.

Taken together, prior results point to two complementary but only partially connected views: (i) time-domain statistics such as EDI and block-energy variability (set by shaping and DM block length), and (ii) frequency-domain structure such as the DC notch/dip and its dependence on block length and symbol rate. What is still missing is a unified framework that *maps concrete statistical descriptors of the energy signal* (mean of the per-block energy variance, variance of the mean energy across blocks, energy variance of the signal, and finite-length constraints) *onto the spectral features* of the intensity-fluctuation PSD that most strongly drive XPM-induced phase noise, *including how these mappings evolve under chromatic dispersion*.

This work bridges this gap by developing an analytical framework that links energy signal statistics directly to the spectral characteristics of the intensity-fluctuation PSD and the resulting XPM-induced phase variance. Specifically, we: (i) derive closed-form expressions quantifying how finite block length, symbol rate, and distribution matching (DM) type (e.g., CCDM vs. ESS) shape low-frequency PSD features via key statistical moments, including the variance of mean block energies and the global energy variance; (ii) incorporate chromatic dispersion to model the spatial evolution of the PSD; and (iii) establish design guidelines to maximize the low-frequency spectral dip and minimize phase variance for specific link lengths. The model is validated against numerical simulations involving shaped QAM waveforms and dispersive propagation, showing excellent agreement with both analytical predictions and prior observations [2], [10]. Ultimately, this framework unifies temporal and spectral perspectives, providing practical criteria for optimizing block length, symbol rate, and shaping algorithms to mitigate fiber nonlinearity.

II. INTENSITY FLUCTUATIONS

A. Fundamentals on Intensity Fluctuations

The optical intensity $I(t)$ is proportional to the magnitude-squared of the optical electric field. For a linearly modulated signal propagating through a dispersive fiber, the intensity evolves as:

$$I(t) \propto \left| A_0 e^{j2\pi f_L t} \cdot \sum_{k=-\infty}^{\infty} a_k s(t - kT) \right|^2 \quad (1)$$

where A_0 is the peak carrier amplitude, f_L is the laser frequency, a_k are zero-mean data symbols, and T is the symbol period. The function $s(t)$ represents the pulse shape $h(t)$ broadened by fiber dispersion, defined as $s(t) = h(t) \otimes \mathcal{F}^{-1}(e^{j\beta\omega^2 z/2})$. The intensity fluctuation (IF) spectrum is obtained via the Fourier transform of (1):

$$|I(f)|^2 \propto |A_0|^4 B_a(f) \quad (2)$$

where $B_a(f)$ is the power spectral density (PSD) of the energy signal of the pulse-shaped data sequence.

For a sequence of independent and identically distributed (i.i.d.), zero-mean data symbols, the energy signal PSD is given by [7]:

$$B_a(f) = \frac{\mu_E^2}{T^2} \sum_l \left| \mathcal{G}\left(\frac{l}{T}, 0\right) \right|^2 \delta\left(f - \frac{l}{T}\right) \quad (3a)$$

$$+ \frac{\sigma_E^2}{T} |\mathcal{G}(f, 0)|^2 \quad (3b)$$

$$+ \frac{2\mu_E^2}{T} \sum_{m \neq 0} |\mathcal{G}(f, mT)|^2 \quad (3c)$$

Here, μ_E and σ_E^2 are the mean and variance of the symbol energy $E = |a|^2$, and $\mathcal{G}(f, \tau)$ is the Fourier transform of the pulse beat function $g(t, \tau) = s(t) \cdot s^*(t - \tau)$. The spectrum comprises discrete lines (3a), a self-beating component (3b), and neighbor-beating components (3c). Since low-frequency IFs in multi-subcarrier systems are dominated by intra-subcarrier beating [7], the single-subcarrier spectrum is sufficient to analyze shaped-constellation performance.

B. Energy Signal PSD for Shaped Data Symbols

When distribution shaping is applied with finite block lengths, the i.i.d. assumption in (3) holds only approximately. Shaping introduces structured energy fluctuations and correlations within blocks. The modified PSD for shaped data symbols with block length n_s is:

$$B_a(f) = \frac{\mu_E^2}{T^2} \sum_l \left| \mathcal{G}\left(\frac{l}{T}, 0\right) \right|^2 \delta\left(f - \frac{l}{T}\right) + \frac{\sigma_E^2}{T} |\mathcal{G}(f, 0)|^2 - \frac{\mu_{\sigma_{\text{blk}}}^2 - (n_s - 1)\sigma_{\mu_{\text{blk}}}^2}{T} |\mathcal{H}(f, 0)|^2 + \frac{2\mu_E^2}{T} \sum_{m \neq 0} |\mathcal{G}(f, mT)|^2 \quad (4)$$

The third term represents the correction due to shaping, where $\mu_{\sigma_{\text{blk}}}^2$ is the average intra-block energy variance and $\sigma_{\mu_{\text{blk}}}^2$ is the variance of the inter-block mean energies. These statistics are derived as follows:

Lemma 1 (Intra-Block Covariance). *The covariance between distinct symbols $i \neq j$ within a block k is:*

$$\text{Cov}(E_i^{(k)}, E_j^{(k)}) = \sigma_{\mu_{\text{blk}}}^2 - \frac{\mu_{\sigma_{\text{blk}}}^2}{n_s - 1}. \quad (5)$$

Proof. Decomposing the symbol energy into the block mean and a deviation, $E_i^{(k)} = \bar{E}^{(k)} + \delta_i^{(k)}$, and noting that deviations $\delta_i^{(k)}$ are uncorrelated with the block mean $\bar{E}^{(k)}$, the covariance expands via the bilinear property:

$$\begin{aligned} \text{Cov}(E_i^{(k)}, E_j^{(k)}) &= \text{Cov}(\bar{E}^{(k)} + \delta_i^{(k)}, \bar{E}^{(k)} + \delta_j^{(k)}) \\ &= \text{Var}(\bar{E}^{(k)}) + \underbrace{\text{Cov}(\bar{E}^{(k)}, \delta_j^{(k)})}_0 \\ &\quad + \underbrace{\text{Cov}(\delta_i^{(k)}, \bar{E}^{(k)})}_0 + \text{Cov}(\delta_i^{(k)}, \delta_j^{(k)}) \\ &= \sigma_{\mu_{\text{blk}}}^2 + \text{Cov}(\delta_i^{(k)}, \delta_j^{(k)}). \end{aligned} \quad (6)$$

Using the constraint that deviations within a block sum to zero ($\sum_{i=1}^{n_s} \delta_i^{(k)} = 0$), the variance of this sum is:

$$\begin{aligned} \text{Var}\left(\sum_{i=1}^{n_s} \delta_i^{(k)}\right) &= \sum_{i=1}^{n_s} \text{Var}(\delta_i^{(k)}) + \sum_{i=1}^{n_s} \sum_{j \neq i}^{n_s} \text{Cov}(\delta_i^{(k)}, \delta_j^{(k)}) \\ &= n_s \mu_{\sigma_{\text{blk}}}^2 + n_s(n_s - 1) \text{Cov}(\delta_i, \delta_j) \\ &= 0. \end{aligned} \quad (7)$$

Solving for $\text{Cov}(\delta_i, \delta_j)$ yields $-\frac{\mu_{\sigma_{\text{blk}}}^2}{n_s - 1}$. Substituting this back into (6) completes the proof.

Lemma 2 (PSD Correction Coefficient). *The per-symbol correction coefficient C_{corr} is:*

$$C_{\text{corr}} = (n_s - 1) \sigma_{\mu_{\text{blk}}}^2 - \mu_{\sigma_{\text{blk}}}^2. \quad (8)$$

Proof. Aggregating the result from Lemma 1 over all $n_s(n_s - 1)$ distinct pairs in a block and normalizing by the block size n_s yields:

$$\begin{aligned} C_{\text{corr}} &= \frac{n_s(n_s - 1)}{n_s} \text{Cov}(E_i^{(k)}, E_j^{(k)}) \\ &= (n_s - 1) \left(\sigma_{\mu_{\text{blk}}}^2 - \frac{\mu_{\sigma_{\text{blk}}}^2}{n_s - 1} \right) \\ &= (n_s - 1) \sigma_{\mu_{\text{blk}}}^2 - \mu_{\sigma_{\text{blk}}}^2 \end{aligned} \quad (9)$$

Remark 1 (Trivial Case $n_s = 1$). *Consider the case where each block contains a single symbol ($n_s = 1$). In this scenario, the block mean is identical to the symbol energy, implying the intra-block deviation is identically zero ($\mu_{\sigma_{\text{blk}}}^2 = 0$). Substituting $n_s = 1$ and $\mu_{\sigma_{\text{blk}}}^2 = 0$ into Lemma 2 causes the correction term to vanish ($C_{\text{corr}} = 0$). This confirms that, for $n_s = 1$, the block-based formulation reduces to the baseline i.i.d.-based PSD model, recovering the original model in (3).*

The function $\mathcal{H}(f, \tau)$ represents the spectral envelope of pulse interactions within a shaped block, defined as the Fourier transform of $p(t, \tau) = u(t)u^*(t - \tau)$. To ensure consistent energy scaling with single pulses, the block envelope $u(t)$ is defined as:

$$u(t) = \frac{1}{\sqrt{n_{\text{norm}}}} \sqrt{\sum_{i=1}^n |s(t - iT)|^2} \quad (10)$$

where n_{norm} is a normalization factor that ensures the total energy of the block envelope $u(t)$ is equivalent to that of a single pulse $s(t)$, satisfying $\int |u(t)|^2 dt = \int |s(t)|^2 dt$.

C. Extension to 2D Shaped Symbols

For 2D symbols (e.g., QAM), shaping may introduce statistical dependence between in-phase (I) and quadrature (Q)

components. The PSD is extended to account for cross-terms arising from $\text{Cov}(I, Q)$:

$$\begin{aligned} B_a(f) &= \frac{\mu_E^2}{T^2} \sum_l \left| \mathcal{G}\left(\frac{l}{T}, 0\right) \right|^2 \delta\left(f - \frac{l}{T}\right) \\ &\quad + \frac{\sigma_E^2}{T} |\mathcal{G}(f, 0)|^2 \\ &\quad - \frac{\mu_{\sigma_{\text{blk}}}^2 - (n_s - 1) \sigma_{\mu_{\text{blk}}}^2}{T} |\mathcal{H}(f, 0)|^2 \\ &\quad + \frac{\Psi_{2D}}{T} \sum_{m \neq 0} |\mathcal{G}(f, mT)|^2 \end{aligned} \quad (11)$$

where the weighting factor Ψ_{2D} is defined as:

$$\Psi_{2D} = \mu_E^2 + (\mu_{I^2} - \mu_{Q^2})^2 + 4\mu_{IQ}^2. \quad (12)$$

Here, $E = I^2 + Q^2$, and μ_{I^2}, μ_{Q^2} denote component powers. The factor Ψ_{2D} explicitly captures power imbalances and I - Q correlations derived from complex random variable properties.

III. SIMULATION SETUP

The analytical models for the energy signal PSD, given in Equations (4) and (11), are first validated against numerical simulations in MATLAB. We investigate two shaping implementations: constant-composition distribution matching (CCDM) and enumerative sphere shaping (ESS). CCDM is a direct shaping method that imposes a fixed target symbol probability distribution, whereas ESS is an indirect method that selects sequences based on a maximum block-energy constraint. Consequently, ESS typically achieves a lower rate loss compared to CCDM for a given shaping rate [3], [21], although it does not directly control the symbol distribution entropy. For validation, shaped QAM symbols are generated, filtered using a root raised cosine (RRC) filter with a roll-off factor of 0.1, and their PSD is computed via the Fourier transform. This framework is further extended to include a fiber dispersion model to verify the analytical predictions in the presence of chromatic dispersion.

Following numerical verification, system-level validation is performed using VPItransmissionMaker Optical Systems v11.5. The transmitter generates shaped QAM symbols, pulse-shaped by an RRC filter with a roll-off of 0.05, and linearly modulated onto an optical carrier with a launch power of 1 mW. The signal propagates through an 80 km Standard Single-Mode Fiber (SSMF) span characterized by a dispersion of 16 ps/nm/km, a nonlinear index of 2.6×10^{-20} m²/W, and an effective area of 80 μm^2 . This setup validates the intensity fluctuation model in Equation (2) and assesses the impact of shaping-induced spectral changes on XPM. The XPM phase fluctuations are isolated using a two-channel configuration with a frequency spacing of 50 GHz and a baud rate of 32 Gbaud. The setup includes a shaped QAM ‘‘inducer’’ channel (1 mW) and a continuous-wave ‘‘victim’’ channel (10 μW) used to capture the phase fluctuations.

IV. NUMERICAL RESULTS

A. Energy Signal PSD of Shaped Symbols

1) Impact of Shaping Methods: In analyzing the energy-signal PSD for shaped QAM symbols and its impact on

nonlinear tolerance, two complementary probabilistic-shaping approaches are commonly used [2], [3], [21]: *direct shaping* and *indirect shaping*. Direct shaping explicitly imposes target symbol probabilities. A practical realization is Constant-Composition Distribution Matching (CCDM), which maps information bits to fixed-length blocks such that the empirical histogram closely follows a prescribed probability mass function (typically Maxwell-Boltzmann) within the limits of finite blocklength. For a QAM alphabet and a block of length n , a composition specifies the frequency of each constellation point; all sequences with that composition are treated as equally likely. This enforces the desired marginal distribution and minimizes inter-block variability in symbol counts. In contrast, indirect shaping does not directly set the probability of symbols. Instead, it selects sequences according to a block-energy constraint: bits are mapped uniformly among all length- n sequences whose total energy (sum of squared symbol magnitudes over the block) lies within a prescribed bound. A variant of this, known as shell mapping, uses an equality constraint. The resulting marginal distribution emerges from the uniform measure on this constrained set and typically approximates an energy-efficient profile.

To verify the energy-signal PSD for shaped QAM symbols, two shaping algorithms are considered: CCDM (using a Maxwell-Boltzmann target distribution) and Enumerative Sphere Shaping (ESS), where shell mapping is applied pragmatically. These methods are compared because their PSD behaviors differ significantly, particularly at low frequencies, as explained in [3]. Fig. 1 illustrates the PSDs of the energy signals for both CCDM and ESS across different block lengths, prior to dispersion. The PSDs are normalized to maintain the same mean energy to allow for direct spectral comparison. The ESS PSD exhibits pronounced energy fluctuations at $f = 0$ Hz for shorter block lengths. In contrast, the CCDM PSD shows consistent behavior across different block lengths, indicating that energy fluctuations are effectively zero at $f = 0$ Hz. Note that the DC component of the PSD is suppressed in these plots, as it has little significance regarding phase noise, generating only fixed phase offsets. The PSDs were generated for a 256-QAM constellation, pulse-shaped using a Root Raised Cosine (RRC) filter with a roll-off factor of 0.1.

2) *Spectral Composition of the Energy Signal PSD*: Equation (11) provides a theoretical framework for calculating the energy signal PSD of shaped QAM symbols. This model accurately reflects the spectral characteristics observed in Fig. 1, including the reduction of low-frequency energy fluctuations due to shaping. The strong agreement between the analytical model and the simulated PSDs confirms the validity of this approach for describing the impact of probabilistic shaping on the energy signal spectrum.

Since the PSD is well described by Equation (11), it can be used to decompose the spectral composition of the energy signal. Based on Equation (11), the spectrum comprises four distinct components:

- **Spectral Lines:** The discrete components of the energy signal (often omitted in analysis focused on fluctuations).
- **Intrinsic Symbol Beating:** The energy resulting from data symbols beating with themselves (the standard con-

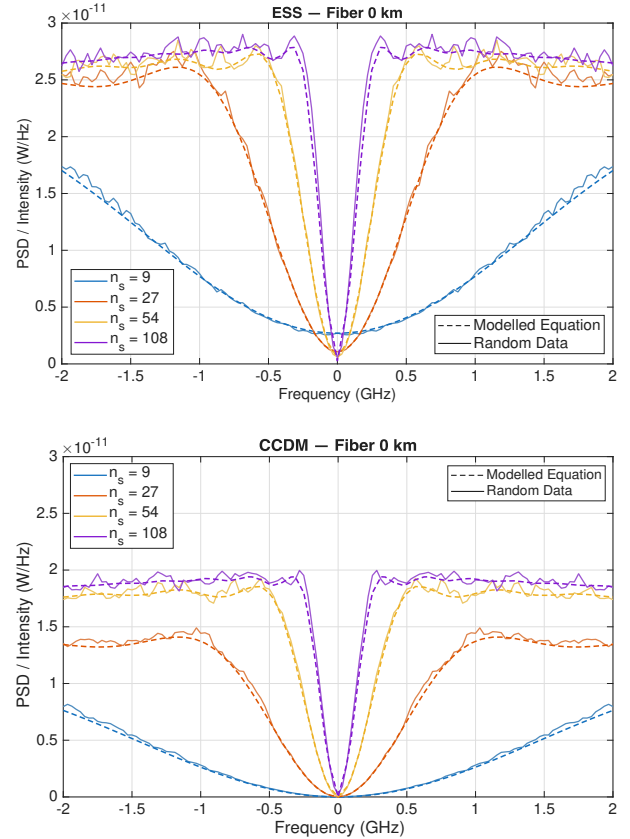


Fig. 1: Energy signal PSDs for shaped QAM symbols: ESS (top) and CCDM (bottom) for different block lengths. The shaped constellations are normalized to have the same mean energy.

tinuous spectrum).

- **Shaping Composition:** A component accounting for the energy variance structure imposed by shaping both across and within blocks.
- **Pulse Overlap/Dispersive Beating:** The energy arising from pulse interactions, which becomes significant with dispersion.

In this analysis, the spectral lines are omitted to focus on low-frequency energy fluctuations. Signal shaping introduces block-based energy variance—reflected in the third component listed above—which is crucial for understanding how shaping alters spectral characteristics. This term effectively reduces the energy fluctuations produced by the self-beating of symbols, which is otherwise the major contributor to low-frequency components below 2 GHz.

Although this composition is analyzed here for an ESS-shaped signal, it is valid for other shaping methods provided the statistical properties outlined in Equation (11) are known. For CCDM-shaped symbols, the variance of the mean energy between blocks is zero ($\sigma_{\mu_{\text{blk}}}^2 = 0$), while the variance of the mean energy within blocks is equivalent to the collective symbol energy variance ($\mu_{\sigma_{\text{blk}}}^2 = \sigma_E^2$). Consequently, energy fluctuations at $f = 0$ Hz are totally suppressed, as evident in Fig. 1. However, for uniformly distributed symbols, the

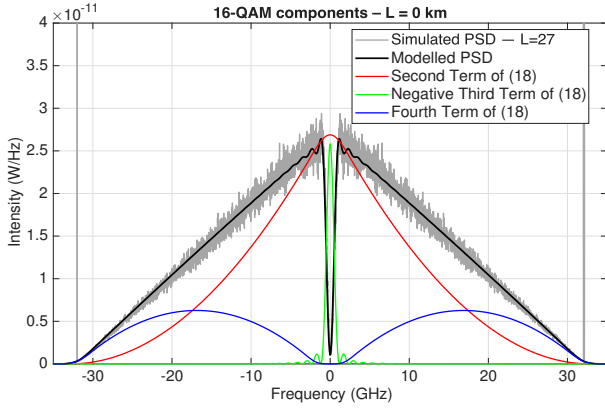


Fig. 2: Spectral composition of the energy signal PSD for ESS shaped QAM symbols with block length of 27, based on Equation (11).

shaping term is negligible; as a result, sub-2 GHz fluctuations persist unless the symbol energy variance is zero (which occurs only in QPSK modulation). This indicates that the shaping process significantly alters the spectral characteristics of the energy signal, particularly at low frequencies.

3) *Impact of Dispersion*: The energy signal PSD is directly proportional to intensity fluctuations, as indicated in Equation (2). Therefore, when the pulse-shaped signals of shaped QAM symbols pass through a dispersion model, the energy signal PSD evolves. This evolution is captured by the model in Equation (11) and illustrated in Fig. 3.

The results clearly show that intensity fluctuations tend to grow with transmission length, consistent with the dispersion model described in Equation (11). The blocklength appears to have an effect similar to the symbol rate, where the PSD level tends to increase with transmission length—a phenomenon well established in [10]. It is important to note that Fig. 3 shows the energy signal PSD, not the final intensity fluctuation spectra; the latter requires appropriate scaling as described in Equation (2). Thus, this section considers only the effect of the dispersion function on pulse-shaped QAM signals.

The rise in the energy signal PSD is primarily caused by increased pulse overlapping due to accumulated dispersion along the fiber. This effect is evident in Fig. 4, which details the spectral composition of the energy signal PSD for ESS-shaped QAM symbols (block length 27) after 640 km. The spectral component corresponding to the fourth term in Equation (11)—the pulse overlap component—has grown significantly compared to the non-dispersed case in Fig. 2, becoming a major contributor to energy fluctuations. While the spectral components due to the second and third terms are still present, their bandwidth is significantly reduced, which is consistent with the pulse broadening effect. However, the peak at $f = 0$ Hz remains unchanged, aligning with findings in [7].

B. Spectral Dip Width

1) *Analytical Formulation*: Having established that the spectral dip arises from the third term in Equations (4) and

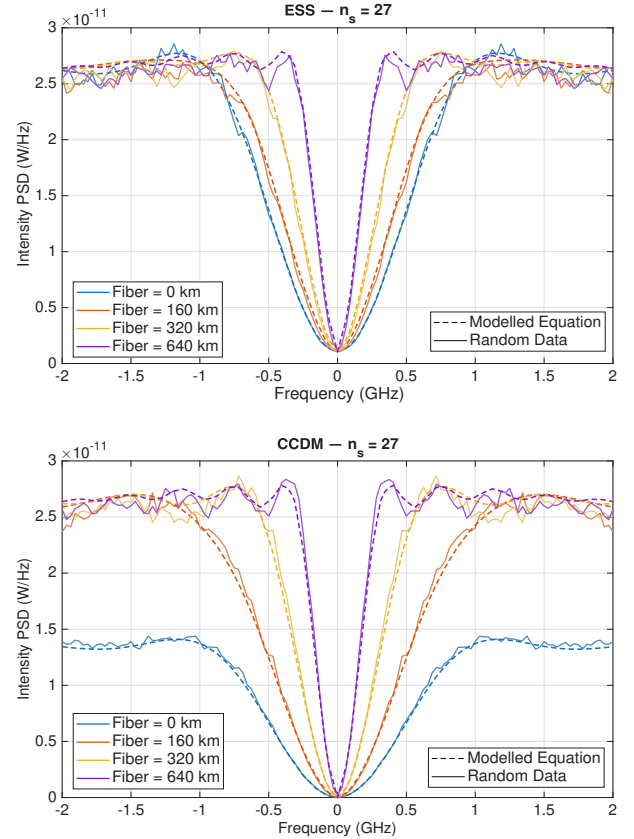


Fig. 3: Energy signal PSDs for shaped QAM symbols: ESS (top) and CCDM (bottom) for different fiber lengths used in the dispersion model. The block length is set to 27 symbols.

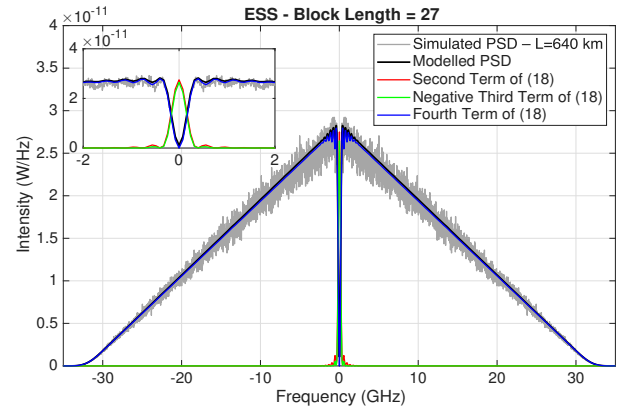


Fig. 4: Spectral composition of the energy signal PSD for ESS shaped QAM symbols with a block length of 27 and fiber length of 640 km, based on Equation (11).

(11), its width can be controlled by adjusting the block length (n_s) and symbol rate (R_s). Before dispersion, the duration of the block envelope is given by:

$$T_b = (n_s - 1 + 2a)T = \frac{n_s - 1 + 2a}{R_s} \quad (13)$$

where $a = t_z R_s$ is the ratio of the pulse's main-lobe half-width (t_z) to the symbol period. For a rectangular pulse, $a = 0.5$;

for an RC pulse, $a = 1$; and for an RRC pulse with small roll-off β , $a \approx 1$. Since the spectral dip at $f = 0$ Hz suppresses the low-frequency intensity fluctuations (IFs) critical for XPM phase noise, controlling its width is essential. As indicated by the inverse relationship in the PSD equations, a longer block length typically narrows this dip.

Chromatic dispersion stretches the block envelope as the signal propagates, further narrowing the spectral dip by reducing the envelope's energy PSD bandwidth. This dispersion-induced narrowing is captured by the broadened block duration T'_b :

$$T'_b = \frac{n_s - 1 + 2a}{R_s} + \kappa_\beta D L R_s \frac{\lambda^2}{c}, \quad (14)$$

Here, D is the dispersion coefficient, L is the fiber length, λ is the wavelength, and c is the speed of light. The factor $\kappa_\beta \approx 1 + \beta$ accounts for the bandwidth expansion due to pulse shaping (e.g., RRC).

The resulting width of the spectral dip is approximately the inverse of the dispersed block duration:

$$\Delta f_b = \frac{2}{T'_b} \quad (15)$$

2) *Dependence on Block Length*: In order to understand how the width of the spectral dip changes with different block lengths, Equation (15) can be used. Keeping the symbol rate constant at 32 Gbaud, the width of the spectral dip is modeled for different block lengths at different fiber lengths. The results are shown in Fig 5, where it can be seen that the width of small block lengths is wider compared to larger block lengths. However, as the fiber length increases, the width of the spectral dip becomes narrower, and at large fiber distances, the width of all block lengths converges to a similar value. This is because the dispersion effect causes the pulse to spread out, which reduces the bandwidth of the energy signal PSD of the envelope.

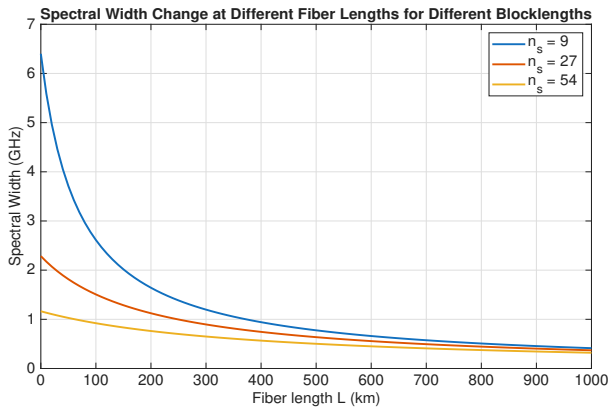


Fig. 5: Modeled width of the spectral dip at $f = 0$ Hz for different block lengths and fiber lengths (symbol rate = 32 Gbaud), based on Equation (15).

3) *Dependence on Symbol Rate*: The width of the spectral dip can also be controlled by adjusting the symbol rate, as described by Equation (15). The results are shown in Fig 6, where it can be seen that as the symbol rate increases, width of the spectral dip becomes wider. However, dispersion

causes significant overlapping between the pulses with high symbol rates, leading to the duration of the block length being stretched proportionally, which can lead to increased low-frequency energy fluctuations. Since dispersion affects different symbol rates differently, it leads to an optimum symbol rate that has the least low-frequency fluctuations. Here, the block length has been kept constant at 18 symbols per block while the symbol rate is varied. The results demonstrated here are valid for any block-based shaping method as long as the statistical properties outlined in Equations (4) and (11) are known.

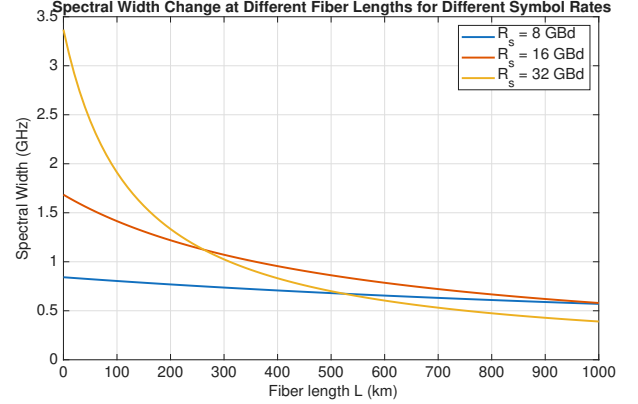


Fig. 6: Modeled width of the spectral dip at $f = 0$ Hz for different symbol rates (block length = 18), based on Equation (15).

C. Optimum Symbol Rate

The optimum symbol rate that maximizes the spectral dip width can be derived by maximizing Δf_b in Equation (15) with respect to R_s . This yields:

$$R_{s,shaped}^{opt} = \sqrt{\frac{(n_s - 1 + 2a)c}{\kappa_\beta D L \lambda^2}} = \sqrt{\frac{n_s - 1 + 2a}{2\pi L |\beta_2| \kappa_\beta}} \quad (16)$$

where $|\beta_2| = D\lambda^2/(2\pi c)$ is the group velocity dispersion parameter.

For the special case of an unshaped system ($n_s = 1$), the model reduces to the dispersion of a single symbol. The optimum rate maximizes the self-beating bandwidth while suppressing low-frequency fluctuations, leading to:

$$R_{s,unshaped}^{opt} = \sqrt{\frac{2ac}{\kappa_\beta D L \lambda^2}} = \sqrt{\frac{a}{\pi L |\beta_2| \kappa_\beta}} \quad (17)$$

This aligns with existing optimal symbol rate formulations in the literature [22], [23], which can be generalized as:

$$R_g = \sqrt{\frac{OL}{2\pi |\beta_2| L_{Link} \nu}} \quad (18)$$

where OL represents the overlap factor and ν accounts for subcarrier spacing. Our derived Equation (17) corresponds to $OL = 2a$ and $\nu = \kappa_\beta$. In comparison, Poggiolini *et al.* [22] propose $OL = 4$ and $\nu = 2\frac{\delta f}{R} - 1$, while Wang *et al.* [23] use $OL = 1$ and $\nu = (\frac{\delta f}{R})^2$.

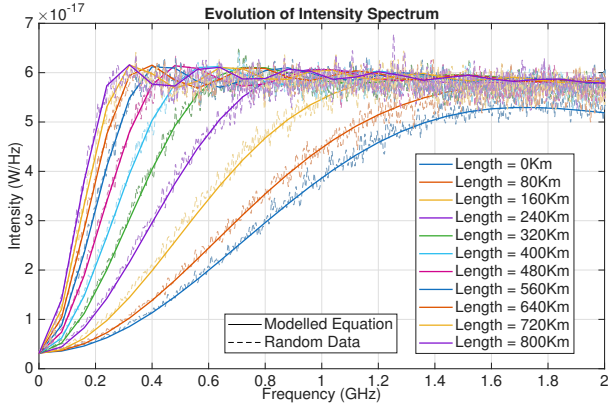


Fig. 7: Intensity fluctuation spectra for a 64-QAM signal transmitted at 32 Gbaud and shaped by the ESS method with a rate of 4.8 bits/symbol and $n_s = 18$. The modeled intensity fluctuation spectra are based on the analytical model presented in Equation (2), and the results are compared against VPItransmissionMaker Optical Systems v11.5 simulation results.

D. Intensity Fluctuations Spectrum

In this section, a full optical simulation is performed to validate the analytical model for intensity fluctuation spectra presented in Equation (2), which serves as the foundation for the XPM phase noise model. While the difference between the energy signal PSD and the intensity fluctuation spectra is negligible, validating Equation (2) is essential as it establishes the critical relationship between intensity fluctuations and XPM phase noise. Fig. 7 presents the modeled intensity fluctuation spectra across various fiber lengths. These results correspond to a 64-QAM signal transmitted at 32 Gbaud, shaped using the ESS method with a rate of 4.8 bits/symbol and $n_s = 18$. As illustrated in Fig. 1, the ESS algorithm applies spectral dip control based on the shaping block length; consequently, unlike the CCDM method, the spectral dip at $f = 0$ Hz is not suppressed. The modeled intensity fluctuation spectra, derived from Equation (2), demonstrate strong agreement with the VPItransmissionMaker Optical Systems v11.5 simulation results, thereby validating the analytical model. As noted in [7], intensity fluctuation spectra at low frequencies are dominated by the beating between neighboring symbols, leading to increased fluctuations in this region; this behavior remains consistent for shaped constellations.

E. XPM Phase Noise

1) *Effect of Shaping Methods:* In the XPM model [15], [24], [25], the phase-noise power spectral density (PSD) is driven by the PSD of data-induced intensity fluctuations. Specifically, the growth of intensity fluctuations at low frequencies (Fig. 7) degrades system performance. Accounting for this growth allows the model to reproduce measured phase-noise spectra and explicitly relates the span-by-span intensity-fluctuation spectrum to the resulting XPM phase noise. Consistent with this, Fig. 8 compares phase-noise spectra for different shaping methods, confirming that the low-frequency region is strongly method-dependent.

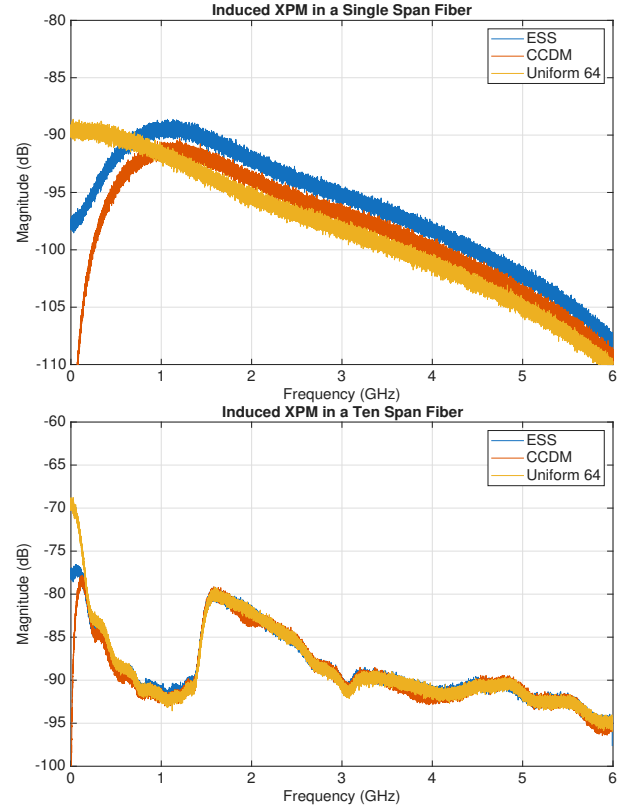


Fig. 8: Phase noise induced on a $10 \mu\text{W}$ probe channel, spaced 50 GHz from a 1 mW pump channel. The phase noise is shown for a single span (top) and a 10-span (bottom) fiber system, demonstrating the filter-like behavior of the XPM transfer function.

For a single-span fiber, the wideband nature of the XPM efficiency function [25] makes the entire bandwidth relevant. However, as the number of spans increases, the contribution of low frequencies becomes dominant [3], [10]. In the ten-span phase fluctuation spectrum shown in Fig. 8, two lobes appear. The first, dominant lobe arises from a sinc-like envelope caused by the coherent vector summation of span-by-span intensity fluctuations—the link efficiency factor [15], [25]—combined with the XPM-efficiency curve. The broader second lobe reflects the finite pass-band of the pump channel, where contributions from a range of frequency separations accumulate to produce a wider response [15].

Fig. 9 compares the phase variance measured on a probe channel for three schemes: unshaped 64-QAM, unshaped 16-QAM, and shaped 64-QAM using ESS and CCDM. Both shaping methods utilize a block size of 18 and a shaping rate of 4.8 bits/symbol. The results demonstrate that probabilistic shaping significantly reduces induced phase variance compared to unshaped signals, with CCDM achieving the lowest phase noise. This superior performance stems from CCDM's ability to suppress low-frequency intensity fluctuations (IFs) near DC, which are the dominant contributors to nonlinear phase noise.

ESS exhibits slightly higher phase variance than CCDM due to residual low-frequency fluctuations. With a finite block

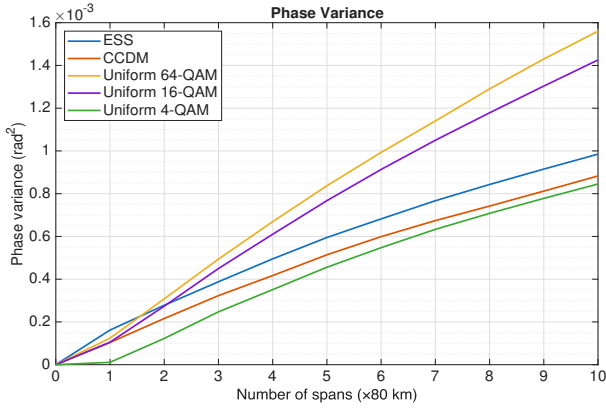


Fig. 9: Comparison of phase variance for unshaped 16-QAM and 64-QAM signals, alongside shaped 64-QAM signals using ESS and CCDM methods (shaping rate 4.8 bits/symbol, block length 18).

length n_s , ESS permits inter-block variability in mean energy, resulting in a non-zero variance of the block mean ($\sigma_{\mu_{\text{blk}}}^2 > 0$). This leaves a finite DC component that CCDM, by virtue of its constant composition design ($\sigma_{\mu_{\text{blk}}}^2 = 0$), suppresses entirely. Although ESS attenuates low-frequency content, it does not fully null the DC component for moderate n_s , particularly when $\mu_{\sigma_{\text{blk}}}^2 \neq \sigma_E^2$ with $\sigma_E^2 > 0$. In practice, the choice of n_s involves a trade-off between residual low-frequency energy (phase variance) and rate loss or computational complexity. As n_s increases, the block-energy distribution concentrates ($\sigma_{\mu_{\text{blk}}}^2 \rightarrow 0$), diminishing the low-frequency pedestal; in the large- n_s regime, the performance gap between ESS and CCDM becomes negligible.

Regarding transmission distance, it is observed that for the first few spans, ESS offers little to no benefit over unshaped 64-QAM or 16-QAM. At short distances, shaping introduces large symbol energy variances, raising the overall intensity fluctuation spectra above that of unshaped signals, as reflected in Equations (4) and (11). However, as the number of spans increases, the balance reverses. Because the XPM efficiency effectively acts as a low-pass filter [2], [10], low-frequency intensity fluctuations eventually dominate the induced phase noise. Since shaping suppresses these specific components, the phase variance for ESS-shaped signals drops below that of unshaped signals after approximately two spans (Fig. 9). Finally, as the modulation order increases, the energy variance of the symbols rises; consequently, the unshaped 64-QAM signal exhibits a stronger intensity fluctuation spectrum and higher phase variance than the unshaped 16-QAM signal.

2) *Effect of Block Length:* As established earlier, block length plays a crucial role in controlling spectral characteristics at lower frequencies (see Fig. 1). Fig. 10 illustrates the phase noise induced on a probe channel by a pump channel using various block lengths for ESS and CCDM shaped 64-QAM signals (4.8 bits/symbol). It is evident that increasing the block length initially raises the phase noise variance on the probe channel over the first 7 spans. Beyond this point, the trend reverses, leading to an optimum block length for minimizing phase variance. This behavior arises because, in

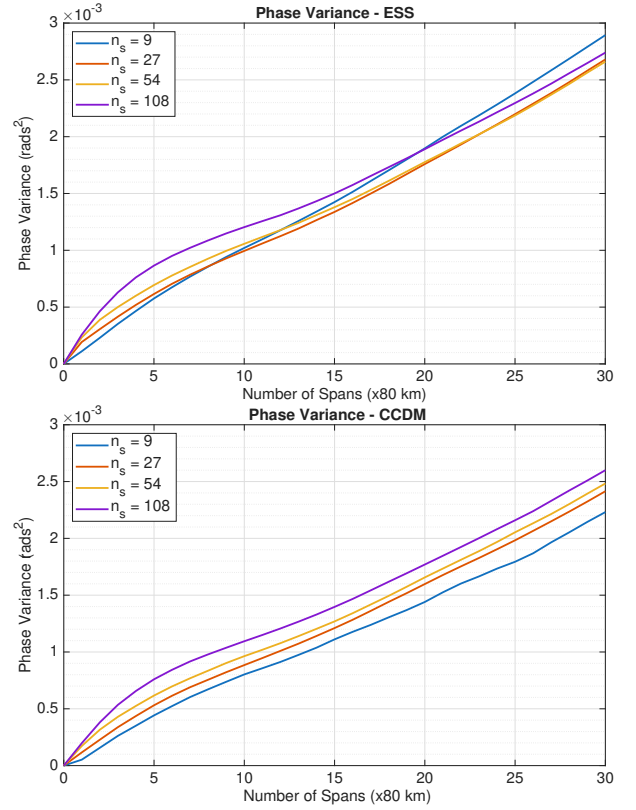


Fig. 10: Phase noise variance induced on a probe channel by a pump channel for different block lengths, using ESS and CCDM methods to shape 64-QAM at a rate of 4.8 bits/symbol.

ESS shaping, longer blocks reduce the depth of the spectral dip while increasing its width at DC. This results in increased intensity fluctuations at low frequencies, which are directly reflected in the XPM phase fluctuation spectra. In contrast, for CCDM, changing the block length affects only the width of the spectral dip, while the depth remains constant (see Fig. 1). As demonstrated in Fig. 5, the spectral dip width for one block length does not cross that of another when the shaping rate is constant. Therefore, phase noise variance depends on both the width and depth of the spectral dip at $f = 0$ Hz, resulting in an optimum block length for ESS shaped signals.

3) *Effect of Symbol Rate:* The symbol rate significantly affects the spectral dip near $f = 0$ Hz and, consequently, the XPM-induced phase noise variance [7]. At shorter transmission distances, a lower symbol rate produces stronger low-frequency intensity fluctuations, leading to higher phase noise on a co-propagating probe channel. However, as the signal propagates, chromatic dispersion broadens the pulses, causing an additional build-up of low-frequency spectral components—an effect known as chirp-induced intensity fluctuations [7] (Figs. 3 and 7). The interplay between intrinsic intensity fluctuations (dominant at low R_s and short distances) and chirp-induced fluctuations (dominant at high R_s and long distances) yields an optimum symbol rate that minimizes total low-frequency noise power [14], [15]. Since XPM-induced phase noise is proportional to these fluctuations, this optimum rate also minimizes phase variance on the probe channel.

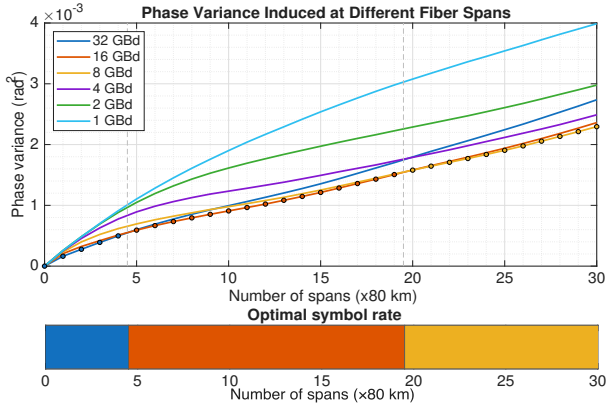


Fig. 11: Phase noise variance induced on a probe channel by a pump channel for different symbol rates using ESS and CCDM shaping methods (64-QAM, shaping rate 4.8 bits/symbol, block length 18).

This trend is demonstrated in Figs. 11 and 12, which plot phase noise variance versus symbol rate for different transmission lengths. Fig. 11 corresponds to an ESS-shaped pump (4.8 bits/symbol, $n_s = 18$), while Fig. 12 uses an unshaped 16-QAM pump. Both scenarios exhibit the same behavior: as transmission length increases, overall phase noise variance grows, and the optimal symbol rate shifts to a lower value. Furthermore, introducing block-based shaping increases the optimum symbol rate. This implies that shaping allows for data transmission at higher symbol rates over longer distances while maintaining lower phase noise variance.

The optimum symbol rate determined via minimum phase variance in Fig. 11 aligns well with the modeled optimum derived in Equation (16) (shown in Fig. 13 for $n_s = 18$). For example, for $N = 3, 10,$ and 27 in Fig. 13, the corresponding optimum symbol rates are approximately 32 Gbaud, 16 Gbaud, and 8 Gbaud, respectively; these match the optima identified in Fig. 11. This validates the modeled optimum symbol rate for shaped signals.

As observed in Fig. 13, the optimum symbol rate increases with block length. This is expected from Equations (14) and (15): longer blocks enlarge intrinsic low-frequency intensity fluctuations, while higher symbol rates generate stronger chirp-induced fluctuations via chromatic dispersion. The operating point minimizing phase noise balances these mechanisms; thus, increasing n_s pushes the optimum R_s upward. As distance grows, the optimum rate for every n_s gradually decreases, and the gap between block lengths narrows, indicating a diminishing benefit of selecting a specific n_s in the long-haul regime. In bandwidth-constrained systems, a large block selection may be suboptimal if its required optimal symbol rate exceeds hardware limitations.

For unshaped signals, the optimum symbol rate determined via Equation (17) follows the trend in Fig. 12 more closely than the equations in [22] and [23]. For $N = 3, 11,$ and 29 in Fig. 14, the approximate optimum rates are 8 Gbaud, 4 Gbaud, and 2 Gbaud, respectively, showing good agreement with Fig. 12. The presented equations offer a middle ground between the results of [22] and [23]. It should be emphasized

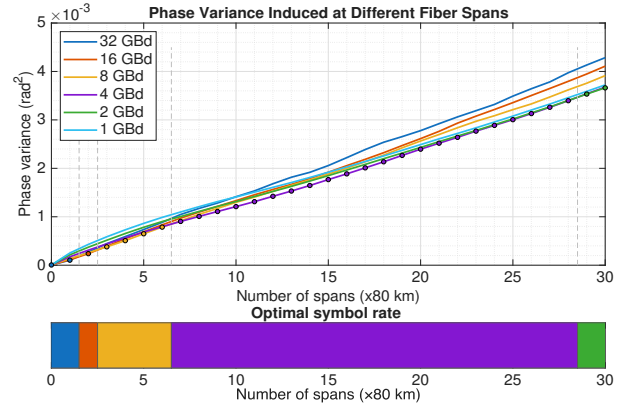


Fig. 12: Phase noise variance induced on a probe channel by a pump channel for different symbol rates using an unshaped 16-QAM signal.

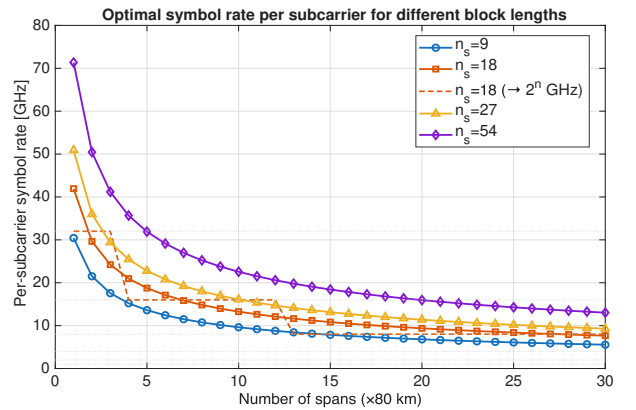


Fig. 13: Optimal symbol rate obtained through Equation (16) with $a \approx 1$ for different block lengths.

that the phase-variance curves in Figs. 11 and 12 are tightly grouped near the transition regions; small uncertainties (e.g., Monte-Carlo averaging or PSD resolution) can shift the selected optimum between neighboring grid values. Therefore, for design purposes, the optimum symbol rate should be interpreted as a narrow range around the theoretical prediction rather than a single exact value.

V. CONCLUSION

This work establishes intensity-fluctuation spectra as a practical design tool for constellation shaping under fiber nonlinearity. Starting from an analytical decomposition of the energy-signal PSD, explicit terms governing low-frequency content were identified: the self-beating contribution, inter-symbol beating across symbol lags, and a block-structure term dependent on the average within-block energy variance ($\mu_{\sigma_{\text{blk}}}^2$) and the variance of the per-block mean energy ($\sigma_{\mu_{\text{blk}}}^2$). These terms explain the contrasting spectral behaviors of CCDM and ESS at $f = 0$ Hz: while CCDM's constant composition suppresses the DC pedestal, ESS exhibits a finite pedestal for moderate block lengths, which decreases as the block energy concentrates with increasing n_s .

A simple width law for the DC spectral dip, $\Delta f_b = 2/T'_b$, was derived, where T'_b incorporates block duration,

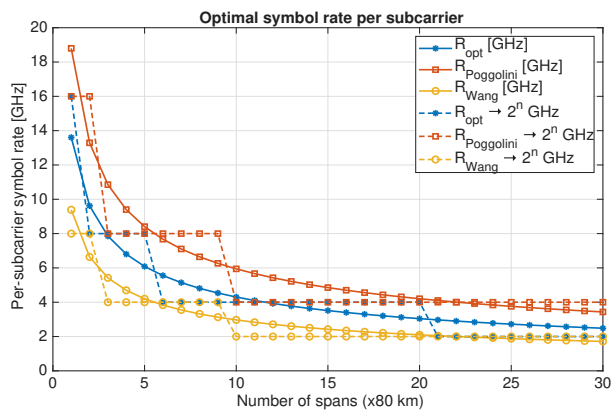


Fig. 14: Optimal symbol rate obtained through Equation (17) with $a \approx 1$, compared with optimal equations derived in [22] ($R_{poggiolini}$) and [23] (R_{wang}).

pulse roll-off, and dispersion. This relationship guides the co-optimization of block length and symbol rate: shorter blocks and moderate rates widen the dip at short distances, while dispersion narrows it during propagation. Based on this trade-off, closed-form expressions for the optimal symbol rate were obtained for both shaped and unshaped systems, showing excellent agreement with the minima of XPM-induced phase variance observed in simulations. The analysis predicts—and the simulations confirm—that shaping reduces phase variance beyond the first few spans. CCDM offers the strongest low-frequency suppression, while ESS approaches this performance as n_s increases. Furthermore, an optimum block length for ESS emerges from the joint control of the width and depth of the spectral dip.

These results yield concrete rules for shaping based on spectral composition to minimise the low-frequency intensity fluctuations that dominate XPM, effectively unifying time-domain energy statistics with frequency-domain PSD features. An explicit symbol-rate rule is provided to achieve the lowest XPM phase noise for both shaped and unshaped systems. The framework readily extends to other shaping methods and modulation formats, offering a practical design pathway for nonlinear-tolerant optical transmission. Future work will focus on extending the framework to multi-channel interactions beyond XPM (e.g., SPM/FWM coupling), polarization-multiplexed 4D shaping with explicit covariance control, and integration with GN/EGN-style system models including ASE noise. Additionally, we will explore the realization of adaptive, distance-aware shaping that tracks dispersion accumulation in real time.

ACKNOWLEDGMENT

The authors express their sincere gratitude to Professor Arthur Lowery for his invaluable guidance, insightful discussions, and constructive feedback throughout the course of this research.

REFERENCES

[1] P. Skvortcov, I. Phillips, W. Forsysiak, T. Koike-Akino, K. Kojima, K. Parsons, and D. S. Millar, “Nonlinearity tolerant lut-based proba-

bilistic shaping for extended-reach single-span links,” *IEEE Photonics Technology Letters*, vol. 32, no. 16, pp. 967–970, 2020.

[2] M. T. Askari and L. Lampe, “Probabilistic shaping for nonlinearity tolerance,” *Journal of Lightwave Technology*, 2024.

[3] A. Amari, S. Goossens, Y. C. Gültekin, O. Vassilieva, I. Kim, T. Ikeuchi, C. M. Okonkwo, F. M. Willems, and A. Alvarado, “Introducing enumerative sphere shaping for optical communication systems with short blocklengths,” *Journal of Lightwave Technology*, vol. 37, no. 23, pp. 5926–5936, 2019.

[4] O. Geller, R. Dar, M. Feder, and M. Shtaif, “A shaping algorithm for mitigating inter-channel nonlinear phase-noise in nonlinear fiber systems,” *Journal of Lightwave Technology*, vol. 34, no. 16, pp. 3884–3889, 2016.

[5] R. Dar, M. Feder, A. Mecozzi, and M. Shtaif, “On shaping gain in the nonlinear fiber-optic channel,” in *2014 IEEE International Symposium on Information Theory*. IEEE, 2014, pp. 2794–2798.

[6] Q. Guo, W.-R. Peng, Y. Cui, and Y. Bai, “Multi-dimensional probabilistic shaping for higher fibre nonlinearity tolerance,” in *45th European Conference on Optical Communication (ECOC 2019)*. IET, 2019, pp. 1–3.

[7] R. Prasad, E. Viterbo, and A. Lowery, “Intensity fluctuations - driving force of nonlinearity in optical fibers,” *Optic Express*, 2025.

[8] O. Vassilieva, I. Kim, H. Irie, Y. Koganei, H. Nakashima, Y. Akiyama, T. Hoshida, and P. Palacharla, “Probabilistic vs. geometric constellation shaping in commercial applications,” in *2022 Optical Fiber Communications Conference and Exhibition (OFC)*. IEEE, 2022, pp. 01–03.

[9] G. Böcherer, F. Steiner, and P. Schulte, “Bandwidth efficient and rate-matched low-density parity-check coded modulation,” *IEEE Transactions on communications*, vol. 63, no. 12, pp. 4651–4665, 2015.

[10] W.-R. Peng, A. Li, Q. Guo, Y. Cui, and Y. Bai, “Baud rate and shaping blocklength effects on the nonlinear performance of super-symbol transmission,” *Optics Express*, vol. 29, no. 2, pp. 1977–1990, 2021.

[11] T. Fehenberger, “On the impact of finite-length probabilistic shaping on fiber nonlinear interference,” in *Signal Processing in Photonic Communications*. Optica Publishing Group, 2020, pp. SpTh11–3.

[12] M. T. Askari, L. Lampe, and J. Mitra, “Probabilistic amplitude shaping and nonlinearity tolerance: Analysis and sequence selection method,” *Journal of Lightwave Technology*, vol. 41, no. 17, pp. 5503–5517, 2023.

[13] T. Fehenberger, D. S. Millar, T. Koike-Akino, K. Kojima, K. Parsons, and H. Griesser, “Analysis of nonlinear fiber interactions for finite-length constant-composition sequences,” *Journal of Lightwave Technology*, vol. 38, no. 2, pp. 457–465, 2020.

[14] L. B. Du and A. J. Lowery, “Optimizing the subcarrier granularity of coherent optical communications systems,” *Optics express*, vol. 19, no. 9, pp. 8079–8084, 2011.

[15] A. J. Lowery and L. Du, “Xpm efficiency versus symbol rate,” *Journal of Light-wave Technology*, vol. 40, no. 9, pp. 2850–2861, 2022.

[16] Z. Chen, J. Zhang, L. Zhong, X. Dai, L. Mei, P. Du, Y. Wang, T. Yang, Q. Yang, and D. Liu, “Penalty mitigation for osc-induced xpm in long-haul wdm coherent systems by digital up-conversion coding,” *Optics Express*, vol. 31, no. 5, pp. 8875–8883, 2023.

[17] J. Zhang, Z. Chen, X. Dai, L. Mei, P. Du, Y. Wang, Q. Yang, and D. Liu, “Xpm phase noise mitigation in long-haul wdm coherent systems by digitally up-converting osc baseband,” in *CLEO: Science and Innovations*. Optica Publishing Group, 2023, pp. SM31–2.

[18] W.-R. Peng, A. Li, Q. Guo, Y. Cui, and Y. Bai, “Transmission method of improved fiber nonlinearity tolerance for probabilistic amplitude shaping,” *Optics Express*, vol. 28, no. 20, pp. 29430–29441, 2020.

[19] K. Wu, G. Liga, A. Sheikh, F. M. Willems, and A. Alvarado, “Temporal energy analysis of symbol sequences for fiber nonlinear interference modelling via energy dispersion index,” *Journal of Lightwave Technology*, vol. 39, no. 18, pp. 5766–5782, 2021.

[20] R. Dar, M. Feder, A. Mecozzi, and M. Shtaif, “Properties of nonlinear noise in long, dispersion-uncompensated fiber links,” *Optics Express*, vol. 21, no. 22, pp. 25685–25699, 2013.

[21] Y. C. Gültekin, W. J. van Houtum, A. G. Koppelaar, and F. M. Willems, “Enumerative sphere shaping for wireless communications with short packets,” *IEEE Transactions on Wireless Communications*, vol. 19, no. 2, pp. 1098–1112, 2019.

[22] P. Poggiolini, A. Nespola, Y. Jiang, G. Bosco, A. Carena, L. Bertignono, S. M. Bilal, S. Abrate, and F. Forghieri, “Analytical and experimental results on system maximum reach increase through symbol rate optimization,” *Journal of Lightwave Technology*, vol. 34, no. 8, pp. 1872–1885, 2016.

- [23] W. Wang, Y. Qiao, and L. Yang, "Detailed discussion of the optimum baud rate of nonlinearity in wdm transmission," *Optics Communications*, vol. 382, pp. 565–573, 2017.
- [24] T.-K. Chiang, N. Kagi, T. K. Fong, M. E. Marhic, and L. G. Kazovsky, "Cross-phase modulation in dispersive fibers: theoretical and experimental investigation of the impact of modulation frequency," *IEEE Photonics Technology Letters*, vol. 6, no. 6, pp. 733–736, 1994.
- [25] T.-K. Chiang, N. Kagi, M. Marhic, and L. G. Kazovsky, "Cross-phase modulation in fiber links with multiple optical amplifiers and dispersion compensators," *Journal of Lightwave Technology*, vol. 14, no. 3, pp. 249–260, 1996.